ACS OMEGA

http://pubs.acs.org/journal/acsodf

Article

Facile Synthesis of MPS_3/C (M = Ni and Sn) Hybrid Materials and Their Application in Lithium-Ion Batteries

Xianyu Liu, Tayyaba Najam, Ghulam Yasin, Mohan Kumar, and Miao Wang*

Cite This: *ACS Omega* 2021, 6, 17247−17254

Read Online

ACCESS | Metrics & More | Article Recommendations | Supporting Information

ABSTRACT: Herein, we successfully synthesized two novel metal thiophosphites (MTPs) hybridized with carbon, that is, $NiPS_3$/C and $SnPS_3$/C composites, via an environment-friendly and cost-effective approach without harsh reaction conditions. Subsequently, the electrochemical performances of $NiPS_3$/C and $SnPS_3$/C composites have been investigated in coin-cells, and it is revealed that MTPs/C have a significantly higher Li-storage capacity and better stability compared to the MTPs without carbon. Moreover, the $SnPS_3$/C electrode shows a lower internal resistance and a better rate performance compared to $NiPS_3$/C. We employed extensive ex situ experiments to characterize the materials and interpreted the remarkably improved performance of MTPs/C.

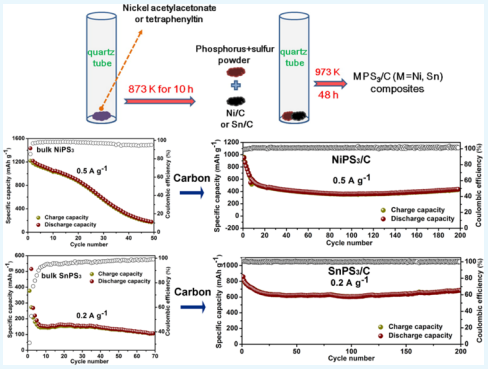

INTRODUCTION

Lithium-ion batteries (LIBs) are considered to be novel substitutes of finite fossil fuels and have been developed very fast in the last few decades. Nowadays, LIBs have been applied widely in energy storage devices, portable electronics, and electric vehicles.[1−5] However, as the present anode material of commercial LIBs, graphite has a low lithiation capacity with a theoretical limitation of 372 mA h g^{-1} and a poor rate performance.[6] Therefore, the research of new anode materials to replace graphite is one of the most attractive topics in LIBs and considerable achievements have been made.[7−11] As reported in previous studies, double-anion MXY (M: metal and X, Y: anion ions) materials have attracted considerable attention and especially have shown some intriguing applications in electrocatalysis.[9−11] Very recently, we synthesized tin phosphides and tin chalcogenides and applied them as the anode materials for LIBs, showing considerably good performances.[12,13] Therefore, for a further step, we attempted to synthesize double-anion MPS_3 (M: Ni and Sn) materials and apply them for LIBs. Previously, metal thiophosphites (MTPs) were also studied as the anode of LIBs.[14−19] For instance, Dangol et al. reported an ultrathin 2D $NiPS_3$ nanosheet electrode that gave a high reversible capacity of 796 mA h g^{-1} at current density of 0.1 A g^{-1}.[16] Du et al. reported a novel graphene-supported $Ni_{0.5}Co_{0.5}PS_3$ nanohybrid that showed a capacity of 456 mA h g^{-1} at 0.5 A g^{-1}.[17] In 2018, Edison et al. for the first time reported novel $SnPS_3$ as the anode of LIBs that delivered 532 mA h g^{-1} at 0.1 A g^{-1}.[18] In contrast, our MPS_3 materials are fabricated in a much simpler way with a large size of ∼10 μm, but showing fairly good lithiation and delithiation properties as anodes of LIBs compared to those nanosized materials reported in the literature, for example, a capacity of 683 mA h g^{-1} over 200 cycles for our $SnPS_3$/C electrode.

As we know, the introduction of carbon could be a useful route to improve the Li-storage properties in LIBs.[20−25] In this work, we provide the first report about successful preparation of two novel $NiPS_3$/C and $SnPS_3$/C composites via a facile two-step process, and applied them as the anodes of LIBs to investigate the lithium storage properties in a coin-cell configuration. For comparison, we also fabricated $NiPS_3$ and $SnPS_3$ without carbon and measured their electrochemical properties. Interestingly, we find that MTPs/C has a significantly higher lithiation capacity and better stability compared to the MTPs without carbon. In order to understand that, we applied X-ray diffraction (XRD), Raman spectroscopy, X-ray photoelectron spectroscopy (XPS), scanning electron microscopy (SEM), and high-resolution transmission electron microscopy (HRTEM) to study the morphologies and structures of MTPs/C. We find that the existence of carbon improves the structural stability of MTP anodes, and also enhances the conductivity and capability of the lithium storage. That is because carbon can serve as a buffer to cushion the stress induced on the anode materials and mitigate the aggregation of the materials during the cycling, as well as

Received: February 25, 2021
Accepted: June 3, 2021
Published: June 29, 2021

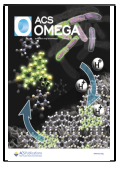

increase the structural stability and enhance the kinetics of charge transfer during the electrochemical process.

In our studies, the $SnPS_3$/C anode shows a lower internal resistance and a better rate performance compared to $NiPS_3$/C, due to a more uniform carbon distribution. In addition, many synthetic pathways such as the chemical vapor transport method, hydrothermal method, chemical exfoliation method, high pressure method, and so forth were utilized to synthesize the abovementioned double-anion TMPC energy nanomaterials, while these synthesis routes have shown some shortcomings, for example, harsh reaction conditions, lack of phase purity, or difficulty in tuning the atomic ratio of the final sample.[16,17,26] Herein, MTPs/C composites were successfully grown in an evacuated quartz tube via a simple high-temperature reaction (see Scheme 1). This kind of confined reaction system utilized here plays a crucial role in the formation of a MTPs/C sample due to a strong inhibition effect on the loss of volatile P and S elements. Compared with conventional synthesis methods for double-anion materials, the facile two-step process employed here for synthesis of MTPs/C shows significant advantages, that is, no complex equipment and harsh reaction conditions.

Scheme 1. Schematic Illustration of Synthetic Routes for MPS_3/C (M = Ni and Sn) Composites

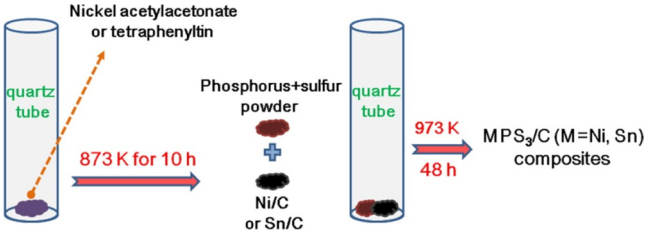

RESULTS AND DISCUSSION

The crystal structures of $NiPS_3$ and $SnPS_3$ are depicted as insets to Figures 1a and 2a. As we have seen, the metal and phosphorus atoms are sandwiched between the layers of sulfur atoms. Note that these materials possess typical van der Waals' layered structures, suitable for application as energy storage materials.[27−29] The XRD patterns for the sample evaluation on phase purity and crystallinity are shown in Figures 1a and 2a: monoclinic $NiPS_3$/C (JCPDS card no. 33-0952, $C2/m$, a = 5.81 Å, b = 10.07 Å, c = 6.63 Å, β = 106.98°); monoclinic $SnPS_3$/C (JCPDS card no. 65-0647, $P2_1/c$, a = 6.55 Å, b = 7.49 Å, c = 11.31 Å, β = 124.19°). Note that quality of XRD patterns for $NiPS_3$/C is better than that for $SnPS_3$/C, in terms of less noise, due to the existence of more carbon in the $SnPS_3$/C composite confirmed by EA analysis and SEM images. Furthermore, the Raman spectrum of $NiPS_3$/C and $SnPS_3$/C samples (Figures 1b and 2b) shows two characteristic peaks located around 1350 and 1600 cm^{-1}, attributed to the G-

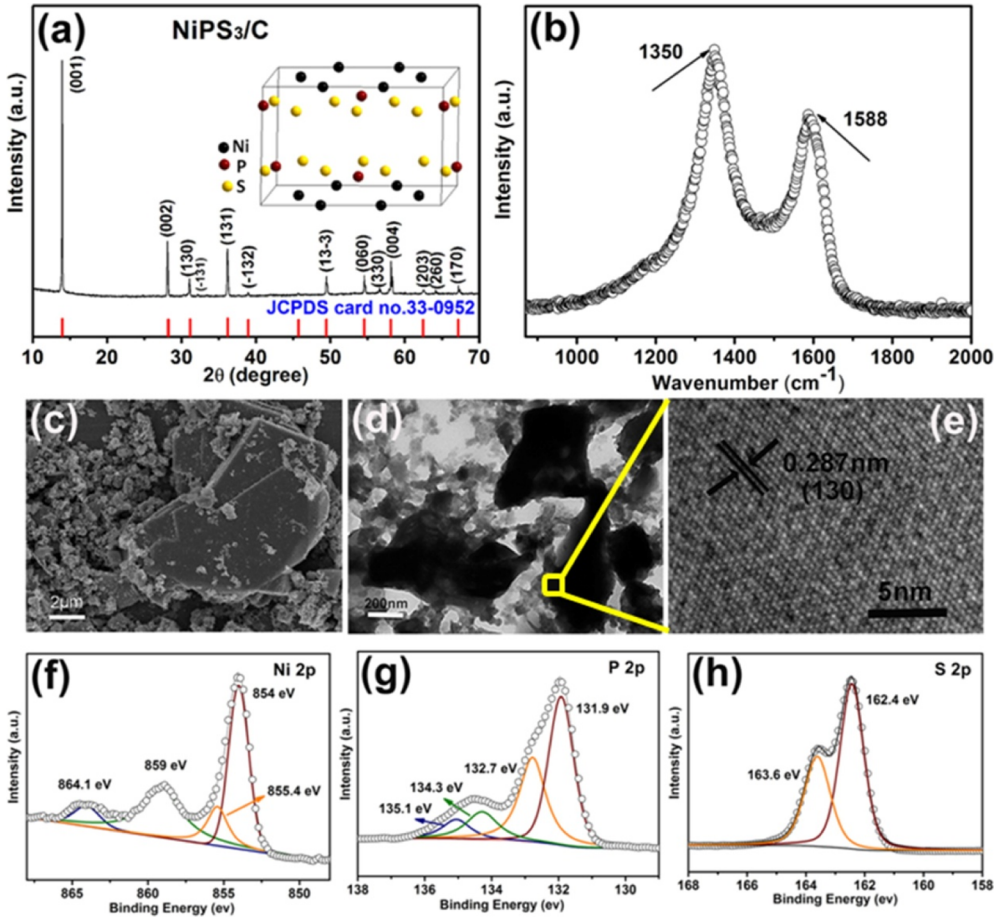

Figure 1. (a) Powder XRD pattern of the $NiPS_3$/C composite. The inset illustrates the crystal structure of $NiPS_3$. (b) Raman spectrum of the $NiPS_3$/C composite. (c) SEM, (d) TEM, and (e) HRTEM images of the $NiPS_3$/C composite. X-ray photoelectron spectral regions for (f) Ni 2p, (g) P 2p, and (h) S 2p levels.

https://doi.org/10.1021/acsomega.1c01042
ACS Omega 2021, 6, 17247−17254

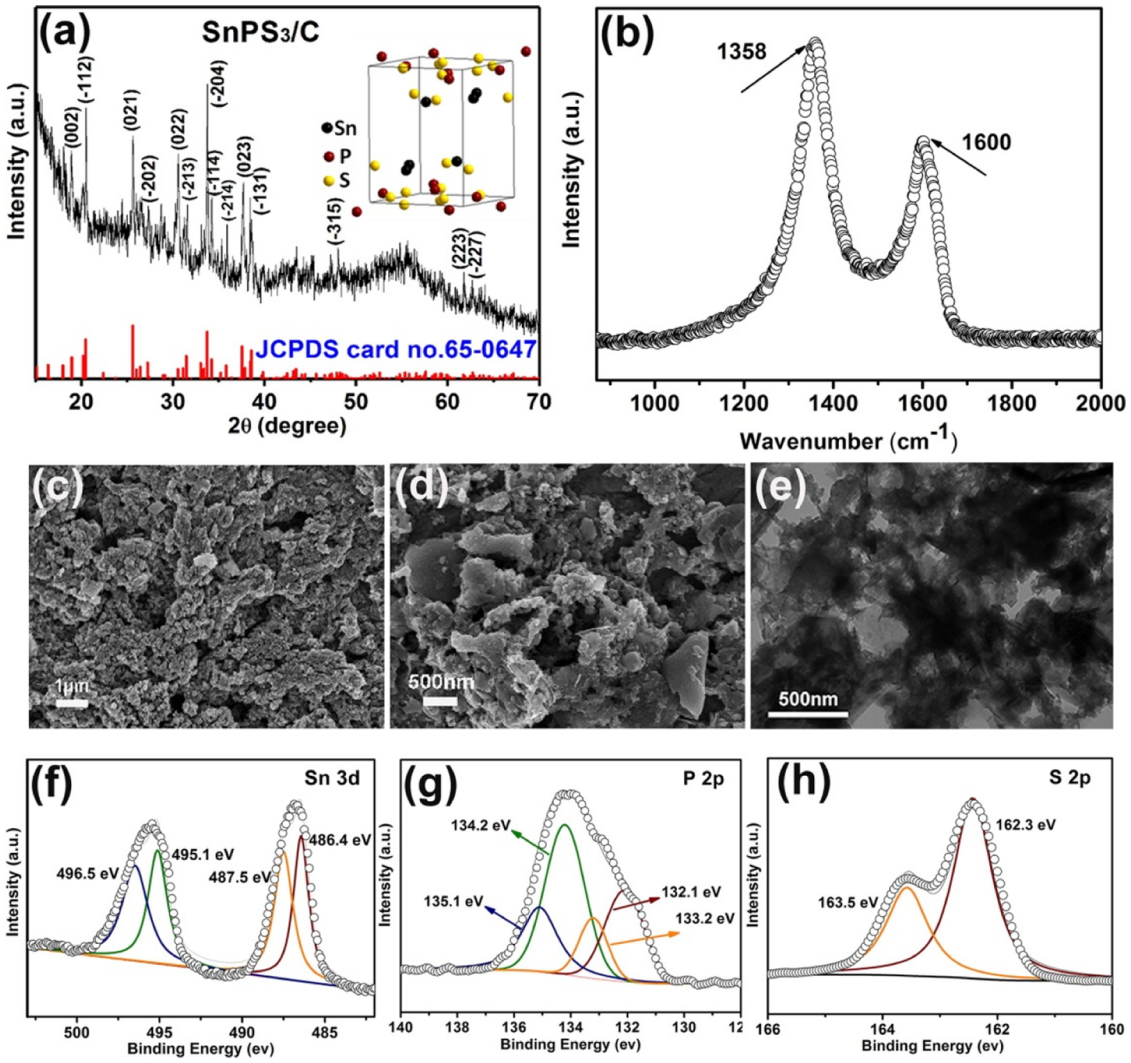

Figure 2. (a) Powder XRD pattern of the $SnPS_3$/C composite. The inset illustrates the crystal structure of $SnPS_3$. (b) Raman spectrum of the $SnPS_3$/C composite. (c) Low-magnified and (d) high-magnified SEM images of the $SnPS_3$/C composite. (e) TEM image of the $SnPS_3$/C composite. X-ray photoelectron spectral regions for (f) Sn 3d, (g) P 2p, and (h) S 2p levels.

and D-bands of carbon, respectively. The G-band corresponds to an E_{2g} vibration mode of carbon and associated with the vibration of carbon sp^2 atoms in a 2D hexagonal lattice, while the D-band is attributed to the vibration of carbon atoms with dandling bonds in plane terminations of disordered carbon. The G- and D-band features confirm that the coated carbon exists as the form of carbon in our samples.[30−32] Elemental analysis reveals that the accurate carbon content of $NiPS_3$/C and $SnPS_3$/C are 9.74 and 15.68 wt %, respectively.

Furthermore, the morphology of the as-synthesized composites was observed using a scanning electron microscope. The microstructure of $NiPS_3$/C shows a feature of typical 2D stacked $NiPS_3$ plates with carbon wrapped around, as shown in Figure 1c. The TEM image (Figure 1d) of the product indicates that the dark $NiPS_3$ is wrapped with carbon, consistent with the SEM image very well. The HRTEM image of the $NiPS_3$/C composite in Figure 1e shows the clear crystal lattice with a d-spacing of 0.287 nm, corresponding to the (130) facet of $NiPS_3$ crystals. XPS was carried out to further analyze the bonding characteristics as well as the composition of as-synthesized samples. The high-resolution XPS spectra shown in Figure 1f reveal a positively charged state of Ni species corresponding to the main peak at ∼854.0 eV, and the other two satellite peaks located at 859.0 and 864.1 eV are of Ni 2p.[33] Specifically, the main positively charged state peak can be resolved into two peaks at 855.4 and 854 eV, attributed to the species of Ni^{3+} and Ni^{2+}, respectively.[34] The P 2p core level XPS spectrum (Figure 1g) has its spin−orbit doublet in the $2p_{3/2}$ and $2p_{1/2}$ peaks positioned at 131.9 and 132.7 eV, respectively, while the peaks situated at 134.3 and 135.1 eV can be ascribed to $2p_{3/2}$ and $2p_{1/2}$ of the P species as a positively charged state.[35] In addition, Figure 1h shows the S 2p spectrum, where S $2p_{3/2}$ and S $2p_{1/2}$ are located at 162.4 and 163.6 eV, respectively.[36,37] The C 1s spectrum is shown in Figure S1 (Supporting Information), where the main peak at 284.8 eV is attributed to the graphitic carbon coating of $NiPS_3$/C and the small peak at ∼286.4 eV is resulted from a slight surface oxidation.[37,38]

The morphology of the as-synthesized $SnPS_3$/C composite was also characterized, and Figure 2c−e shows the representative SEM and TEM images of the $SnPS_3$/C composite with different magnifications. It is found that the microstructure of the $SnPS_3$/C composite shows an irregular aggregation between the matrix and carbon as compared to the

https://doi.org/10.1021/acsomega.1c01042
ACS Omega 2021, 6, 17247−17254

$NiPS_3$/C composite, due to the existence of more carbon in the $SnPS_3$/C composite. Figure S2 depicts the corresponding EDX mapping characterization of the as-synthesized $SnPS_3$/C composite, and the images confirm the uniform distributions of tin, phosphorus, and sulfur elements, which are evenly encapsulated in the carbon layers. Figure 2f shows the XPS spectrum of the Sn 3d level, where the species at 486.4 and 495.1 eV are assigned to Sn^{2+} $3d_{5/2}$ and $3d_{3/2}$, while the other two species at 487.5 and 496.5 eV are assigned to the more positive state of the Tin element, such as Sn^{3+}.[39] Figure 2g shows the P 2p spectrum. The outline of our P 2p spectrum is very similar to that of the $SnPS_3$ material synthesized by Edison et al.[18] However, the fitting of P 2p in Edison et al.'s work is obviously wrong as the intensity of the P $2p_{1/2}$ peak is much higher than that of the P $2p_{3/2}$ peak, but actually the intensity of P $2p_{1/2}$ should be a half of that of P $2p_{3/2}$. We fit the P spectrum correctly in our work as four species, assigned to two groups of $2p_{3/2}$ and $2p_{1/2}$ doublets shown in Figure 2g, where the intensity of $2p_{1/2}$ is exactly a half of that of $2p_{3/2}$.[35] Edison et al. made the similar mistake for S 2p fitting as well, where the S $2p_{1/2}$ is much bigger than S $2p_{3/2}$.[18] In Figure 2h, our S 2p spectrum shows a correct fitting, where the S $2p_{3/2}$ and $2p_{1/2}$ peaks are located at 162.3 and 163.5 eV, respectively, and the lower binding energies indicate a negatively charged S species in our $SnPS_3$/C sample. Thus, it is indicated that the charges transfer from the Sn and P elements to S in the $SnPS_3$/C composite.[36,37] Figure S3 in Supporting Information shows C 1s of $SnPS_3$/C, very similar to that of $NiPS_3$/C.

The suitability of the $NiPS_3$/C composite to host Li ions was studied in half-cell configurations in a coin-cell assembly. The electrochemical properties of the as-synthesized product were further tested by cyclic voltammetry (CV) between 0.01 and 3.00 V at a scan rate of 0.1 mV s^{-1}, and the initial five consecutive cycles are shown in Figure 3a. The cyclic voltammogram reveals the initial lithiation and conversion reaction of the $NiPS_3$/C electrode occurring at a voltage of 1.7 and 1.1 V versus Li/Li^+ in the first cathodic cycle. In the anodic scanning curve, three oxidation peaks located at 1.3, 1.9, and 2.3 V correspond to the lithium-ion delithiation reaction.[40−42] From the charge−discharge voltage profiles of the $NiPS_3$/C composite electrode at 0.5 A g^{-1} in the potential range of 0.01−3.00 V (vs Li/Li^+) for the 1st, 2nd, 3rd, and 100th discharge−charge cycles (Figure 3b), an obvious platform at ∼1.2 V can be observed in the first discharge process, consistent with the above CV data. During the first charge process, a step located at 2.2 V is observed, followed by plateaus moving to higher potential gradually in the subsequent cycles. Figures 3c and S4 display the representative cycling performance of the $NiPS_3$/C composite electrode and $NiPS_3$ electrode at a specific current of 0.5 A g^{-1}, respectively. The capacities and currents were calculated based on the mass of $NiPS_3$/C and $NiPS_3$ anode materials in the electrode. The $NiPS_3$/C composite electrode exhibits a capacity of about 441 mA h g^{-1} over 200 cycles (Figure 3c), while the $NiPS_3$ electrode shows sustained capacity fading during the electrochemistry cycling process and decreased to 172 mA h g^{-1} after 50 cycles (Figure S4). In comparison to the $NiPS_3$ electrode, the $NiPS_3$/C electrode evidently shows a better electrochemical performance. As for the initial capacity fading trend of the $NiPS_3$/C electrode (Figure 3c), it is likely due to the capacity losses incurred by the degradation of active materials in the electrolyte during the cycling process. The corresponding electrochemical mechanism for the $NiPS_3$ electrode has been reported in previous literature: $NiPS_3 + xLi^+ + xe^- \leftrightarrow Li_xNiPS_3$, $Li_xNiPS_3 + yLi^+ + ye^- \rightarrow 3Li_2S + Ni + P$ and $P + yLi^+ + ye^- \rightarrow Li_yP$.[14,15] Figure S5 in Supporting Information depicts the excellent rate capability of the $NiPS_3$/C composite electrode, although the cycling stability could be further improved. Recently, Dangol et al. reported ultrathin 2D $NiPS_3$ nanosheets that were obtained by liquid-phase exfoliation, which showed a high reversible capacity of 796 mA h g^{-1} at a current density of 0.1 A g^{-1} after 150 cycles.[16] Moreover, Du et al. reported a novel graphene-supported $Ni_{0.5}Co_{0.5}PS_3$ nanohybrid electrode that shows a capacity of 456 mA h g^{-1} after 500 cycles at 0.5 A g^{-1},[17] which is comparable to that of the $NiPS_3$/C composite electrode in this work.

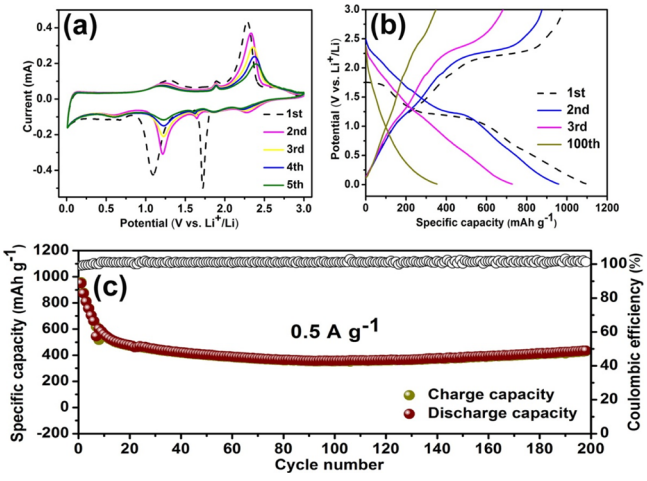

Figure 3. (a) First five voltammograms of the $NiPS_3$/C composite electrode in the voltage ranging from 0.01 to 3 V at a scan speed of 0.1 mV s^{-1}. (b) Galvanostatic charge−discharge curves of the $NiPS_3$/C composite electrode at a current density of 0.5 A g^{-1}. (c) Cycling performance of the $NiPS_3$/C composite electrode at a current density of 0.5 A g^{-1}.

Similarly, the electrochemical performance of the $SnPS_3$/C composite was also investigated in half-cell configurations in a coin-cell assembly. The first five consecutive CVs (Figure 4a) of the $SnPS_3$/C composite electrode were collected. For the first cycle, two reduction peaks can be found at 1.6 and 1.2 V, attributed to the initial lithiation and conversion reaction of Li with $SnPS_3$.[18,40−42] The irreversible reduction peak at 0.75 V can be ascribed to the reaction between the active materials and the electrolyte for the formation of a solid electrolyte interface membrane.[33,41,42] During the subsequent positive sweep, the oxidation peak located at 2 V corresponds to lithium-ion delithiation reaction. From the second cycle, the CV curves mostly overlap, indicating a good reversibility for the $SnPS_3$/C electrode during the electrochemical reactions. The discharge and charge curves for the 1st, 2nd, 3rd, 10th, and 100th cycles at a current density of 0.2 A g^{-1} are shown in Figure 4b. Consistent with the above CV results, a platform at 1.25 V is observed in the discharge process. In the charge process, a weakening plateau situated at 1.7 V can be observed. Notably, the reaction mechanism of $SnPS_3$ toward lithium also has been confirmed by earlier report: $SnPS_3 + xLi^+ + xe^- \rightarrow Li_xSnPS_3$, $Li_xSnPS_3 + yLi^+ + ye^- \rightarrow 3Li_2S + Sn + P$, $Sn + xLi^+ + xe^- \leftrightarrow Li_xSn$ and $P + yLi^+ + ye^- \leftrightarrow Li_yP$.[18] Figures 4c and S6 display the cyclic performance of the $SnPS_3$/C composite and $SnPS_3$ electrodes at a current density of 0.2 A g^{-1}, respectively. The capacities and currents were calculated based on the mass

https://doi.org/10.1021/acsomega.1c01042
ACS Omega 2021, 6, 17247−17254

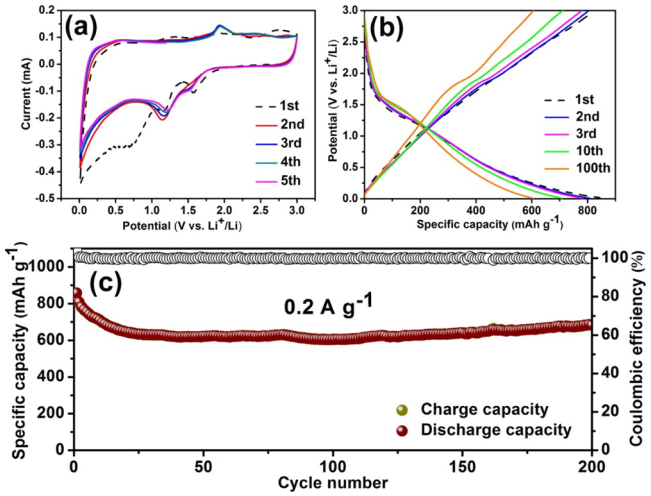

Figure 4. (a) First five voltammograms of the $SnPS_3$/C composite electrode in the voltage ranging from 0.01 to 3 V at a scan speed of 0.1 mV s^{-1}. (b) Galvanostatic charge−discharge curves of the $SnPS_3$/C composite electrode at a current density of 0.2 A g^{-1}. (c) Cycling performance of the $SnPS_3$/C composite electrode at a current density of 0.2 A g^{-1}.

of the corresponding anode materials in the electrode. The $SnPS_3$/C composite electrode delivers a capacity of about 683 mA h g^{-1} over 200 cycles, indicating that the $SnPS_3$/C electrode shows a significantly enhanced cycling performance than the $SnPS_3$ electrode. As seen in Figure S6, the $SnPS_3$ electrode initially experiences a sharp capacity fading and only maintains a capacity of 108 mA h g^{-1} over 70 cycles. It is worth noting that an observable downward trend related to the delivered capacity of the $SnPS_3$/C composite electrode could be mainly due to volume expansion accompanying the Li-alloying electrochemical process occurring in the electrode. The rate performance of the $SnPS_3$/C electrode is distinctly better than that of the $NiPS_3$/C electrode, as shown in Figure S7 in Supporting Information. Note that Edison et al. recently reported a $SnPS_3$ anode that delivered a capacity of 532 mA h g^{-1} after 100 cycles at a current density of 0.1 A g^{-1}.[18] It is significant that the $SnPS_3$/C composite electrode in this work displays better specific capacitance as well as cycling stability during the charge−discharge process compared to Edison et al.'s work. Based on the above analysis, we can find that both $NiPS_3$/C and $SnPS_3$/C composite electrodes display a significantly higher lithiation capacity and better cycling stability compared to the corresponding MTPs without carbon in our experiments. It is because carbon serves as a buffer to cushion the stress induced on the anode and mitigates the aggregation of the materials during the cycling, thus enhancing the stability of the anode. Simultaneously, the electrons involved in electrochemical reactions can easily penetrate the carbon during the lithiation and delithiation, leading to excellent conductivity.

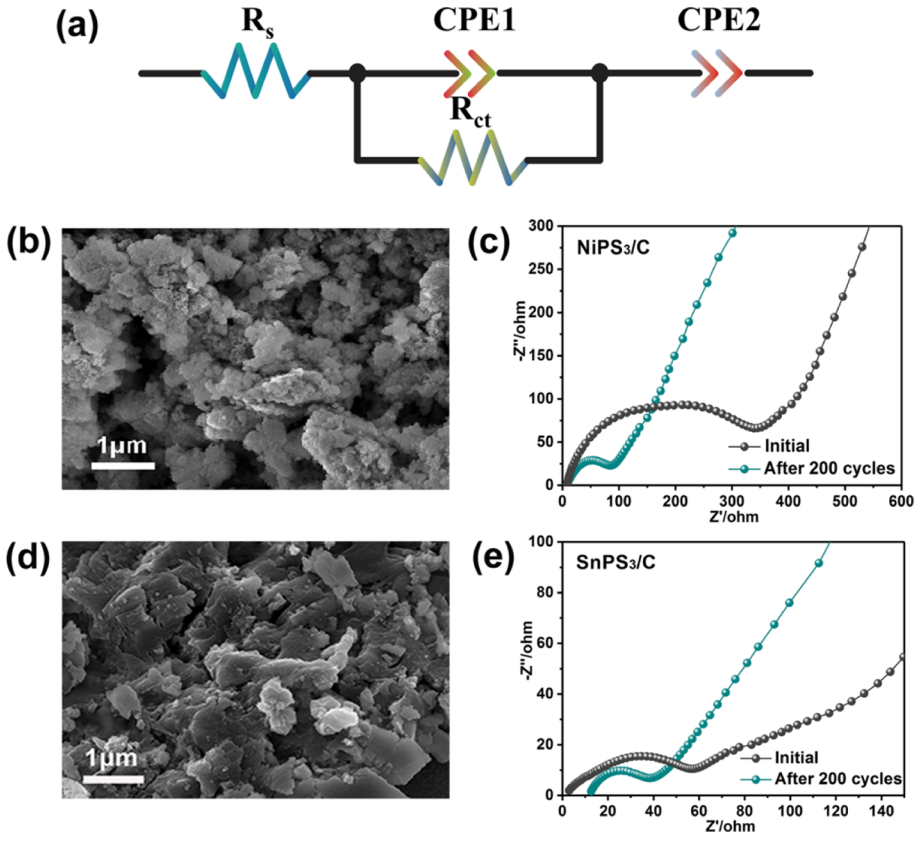

Figure 5. (a) Equivalent circuit model to fit the Nyquist plots, R_s: contact resistance between the electrode and the electrolyte; R_{ct}: charge transfer resistance; and CPE: constant phase element. (b) SEM image of the $NiPS_3$/C composite electrode after 200 cycles at 0.5 A g^{-1} and (c) electrochemical impedance spectra of the $NiPS_3$/C composite electrode before cycling and after 200 cycles at 0.5 A g^{-1}. (d) SEM image of the $SnPS_3$/C composite electrode after 200 cycles at 0.2 A g^{-1} and (e) electrochemical impedance spectra of the $SnPS_3$/C composite electrode before cycling and after 200 cycles at 0.2 A g^{-1}.

https://doi.org/10.1021/acsomega.1c01042
ACS Omega 2021, 6, 17247−17254

In order to further understand the electrochemical performances of the $NiPS_3$/C composite and $SnPS_3$/C composite electrodes, electrochemical impedance spectroscopy (EIS) was applied to investigate the conductivity change of the as-prepared composite electrode before charge−discharge cycling and after 200 cycles. Figure 5a displays the equivalent circuit model, where R_s is the internal resistance between the electrolyte and the electrode; CPE and R_{ct} correspond to the constant phase element and charge transfer resistance, respectively. The Nyquist plots of the as-prepared composites are shown in Figure 5c,e. Specifically, the semicircle located in the medium frequency region in the Nyquist plots is associated with internal resistances of the electrode.[43] Therefore, clearly the $NiPS_3$/C and $SnPS_3$/C composite electrodes show an observable impedance decrease after 200 cycles compared to that before cycling, suggesting that the as-prepared composites maintain good electron-transport during the cycling process.[33] This may be attributed to the existence of carbon in the composites.[44] Meanwhile, the ex situ SEM is carried out to study the structural change of the composite electrodes after 200 cycles. From the ex situ SEM images (Figure 5b,d), we can see that these two composites show an irregular morphology after cycling, inducing improved electron-transport properties due to the good contact between $NiPS_3$ (or $SnPS_3$) and carbon. Note that electrochemical experiments show that $SnPS_3$/C (Figure S7) is better than the $NiPS_3$/C (Figure S5) composite in terms of the delivered Li-storage capacity. From the SEM images, it is found that the integration of the carbon and $SnPS_3$ is higher than that of $NiPS_3$ and C, thus a better conductivity for $SnPS_3$/C during the charge−discharge process of Li-ion batteries. This also is evidenced by EIS investigations as shown in Figure 5c,e, clearly suggesting a lower internal resistance for the $SnPS_3$/C electrode compared to the $NiPS_3$/C electrode, thus more excellent electrochemical properties for the $SnPS_3$/C electrode.

CONCLUSIONS

In this work, we utilized an environment-friendly and cost-effective route for the synthesis of two novel $NiPS_3$/C and $SnPS_3$/C composites. Taking advantage of the carbon layer, the MTPs/C composites show obviously enhanced Li-storage properties than the corresponding unmodified MTPs. Specifically, the $NiPS_3$/C composite electrode delivers a specific capacity of 441 mA h g^{-1} after 200 cycles at a current density of 0.5 A g^{-1}, while the $SnPS_3$/C composite electrode shows 683 mA h g^{-1} over 200 cycles at 0.2 A g^{-1}, respectively. A better rate performance for the $SnPS_3$/C electrode compared to $NiPS_3$/C is because the aggregation between $SnPS_3$ and carbon is more homogeneous than that in the $NiPS_3$/C composite, therefore a better conductivity for $SnPS_3$/C. Moreover, ex situ EIS as another proof also showed lower internal resistances for the $SnPS_3$/C electrode than the $NiPS_3$/C electrode. These results highlight the introduction of carbon as the strategy to achieve high-performance anodes for LIBs and also help us to understand the mechanism behind.

EXPERIMENTAL SECTION

Materials. Nickel acetylacetonate [Ni(acac)2, 95% purity], tetraphenyltin [$Sn(C_6H_5)_4$, 97% purity], red phosphorous [98.5% purity], and sublimate sulfur [99.95% purity] were purchased from Aladdin Company. The solvent, ethanol, was obtained from Shanghai Chemical Reagents Company, China. All reagents were used as received without further purification.

Sample Synthesis. MPS_3/C (M = Ni, Sn) composites were grown via a facile two-step technical route. In a typical procedure, powder of nickel(II) acetylacetonate (95%) or tetraphenyltin (97%) was loaded into sealed quartz tubes, and heated at 873 K for 10 h. Then, the dark precipitates of Ni/C and Sn/C were collected without any purifying treatment. Stoichiometric amounts of Ni/C (or Sn/C), red phosphorus (99%), and sublimated sulfur (99%) were thoroughly mixed together in proportion, and encapsulated in evacuated quartz ampoules, then followed by a sintering procedure at 973 K for 2 days. Scheme 1 schematically illustrates the synthesis route for MPS_3/C (M = Ni, Sn) composites. After the furnace cooled down to room temperature naturally, the products were harvested carefully, washed with absolute alcohol several times, and dried in a vacuum furnace at 60 °C for subsequent characterization.

Structural Characterization. The phases and purity of the obtained products were characterized by X-ray powder diffraction on a Philips X'pert X-ray diffractometer equipped with Cu Kα radiation (λ = 1.5418 Å). The SEM images were obtained using a JEOL-JSM-6700F field-emission scanning electron microscope. The TEM images and HRTEM images were obtained on a JEOL-2010 with an acceleration voltage of 200 kV, and the samples for analysis were prepared by dipping carbon-coated copper grids into ethanol-dissolved samples, then dried under ambient conditions. XPS was performed on a Thermo ESCALAB 250. Raman spectroscopy was carried out on a JY LABRAM-HR confocal laser micro-Raman spectrometer using Ar^+ laser excitation with a wavelength of 514.5 nm. The elemental ratios of Ni, Sn, P, and S were derived from XPS analysis. The weight percentage of carbon was analyzed by elemental analysis (EA, Elemental vario EL cube, Thermal Conductivity Detector) in a pure oxygen atmosphere.

Electrochemical Characterization. Coin-type 2016 cells were assembled in an argon-filled glovebox (O_2, H_2O < 1 ppm) with lithium foil as the anode, Celgard 2400 as the separator, and 1.0 M $LiPF_6$ in ethylene carbonate (EC)/diethyl carbonate (DEC) (1:1 by volume) as the electrolyte. The working electrode was prepared by mixing active materials, carbon black, and polyvinylidene fluoride in a weight ratio of 6:2:2 in *N*-methyl-2-pyrrolidone. Then, the mixture was ball-milled for 10 h to mix uniformly, then the obtained slurry was spread on a Cu foil substrate and dried at 80 °C in a vacuum oven for 10 h. The loading mass of the $NiPS_3$/C and $SnPS_3$/C anode materials is around 1−1.5 mg. Galvanostatic measurements were performed using a LAND-CT2001A instrument in the potential range of 0.01−3 V (*vs* Li/Li^+) at a designated current density at constant room temperature. CV was performed at a scan rate of 0.1 mV s^{-1} with an electrochemical workstation (CHI660E).

ASSOCIATED CONTENT

Supporting Information

The Supporting Information is available free of charge at https://pubs.acs.org/doi/10.1021/acsomega.1c01042.

XPS region for C 1s level of the $NiPS_3$/C composite; SEM image of the $SnPS_3$/C composite and the corresponding element mapping distributions (C, Sn, P, and S); C 1s spectrum of the $SnPS_3$/C composite; XPS region for the C 1s level of the $SnPS_3$/C composite;

https://doi.org/10.1021/acsomega.1c01042
ACS Omega 2021, 6, 17247−17254

cycling performance of the $NiPS_3$ electrode at a current density of 0.5 A g^{-1}; rate capability of the $NiPS_3$/C composite electrode at current densities ranging from 0.1 A g^{-1} to 2 A g^{-1}; cycling performance of the $SnPS_3$ electrode at a current density of 0.2 A g^{-1}; and rate capability of the $SnPS_3$/C composite electrode at current densities ranging from 0.1 A g^{-1} to 2 A g^{-1} (PDF)

AUTHOR INFORMATION

Corresponding Author

Miao Wang − *Institute for Advanced Study, Shenzhen University, Shenzhen 518060, China; College of Physics and Optoelectronic Engineering, Shenzhen University, Shenzhen 518060, China*; Email: wm306@szu.edu.cn

Authors

Xianyu Liu − *School of Chemistry and Chemical Engineering, Lanzhou City University, Lanzhou 730070, China*; orcid.org/0000-0003-3087-0368

Tayyaba Najam − *Institute for Advanced Study, Shenzhen University, Shenzhen 518060, China; College of Physics and Optoelectronic Engineering, Shenzhen University, Shenzhen 518060, China*; orcid.org/0000-0002-9284-9401

Ghulam Yasin − *Institute for Advanced Study, Shenzhen University, Shenzhen 518060, China; College of Physics and Optoelectronic Engineering, Shenzhen University, Shenzhen 518060, China*; orcid.org/0000-0001-8794-3965

Mohan Kumar − *Institute for Advanced Study, Shenzhen University, Shenzhen 518060, China; College of Physics and Optoelectronic Engineering, Shenzhen University, Shenzhen 518060, China*

Complete contact information is available at: https://pubs.acs.org/10.1021/acsomega.1c01042

Notes

The authors declare no competing financial interest.

ACKNOWLEDGMENTS

This work was supported by the Doctoral Research Fund of Lanzhou City University (LZCU-BS2020-03).

REFERENCES

(1) Scrosati, B.; Hassoun, J.; Sun, Y.-K. Lithium-ion batteries. A look into the future. *Energy Environ. Sci.* **2011**, *4*, 3287−3295.

(2) Manthiram, A.; Song, B.; Li, W. A perspective on nickel-rich layered oxide cathodes for lithium-ion batteries. *Energy Storage Mater.* **2017**, *6*, 125−139.

(3) Xu, Q.; Li, J.-Y.; Sun, J.-K.; Yin, Y.-X.; Wan, L.-J.; Guo, Y.-G. Watermelon-inspired Si/C microspheres with hierarchical buffer structures for densely compacted lithium-ion battery anodes. *Adv. Energy Mater.* **2017**, *7*, 1601481.

(4) Zhang, H.; Huang, X.; Noonan, O.; Zhou, L.; Yu, C. Tailored yolk-shell Sn@C nanoboxes for high-performance lithium storage. *Adv. Funct. Mater.* **2017**, *27*, 1606023.

(5) Zuo, X.; Zhu, J.; Müller-Buschbaum, P.; Cheng, Y.-J. Silicon based lithium-ion battery anodes: A chronicle perspective review. *Nano Energy* **2017**, *31*, 113−143.

(6) Huo, K.; Wang, L.; Peng, C.; Peng, X.; Li, Y.; Li, Q.; Jin, Z.; Chu, P. K. Crumpled N-doped carbon nanotubes encapsulated with peapod-like Ge nanoparticles for high-rate and long-life Li-ion battery anodes. *J. Mater. Chem. A* **2016**, *4*, 7585−7590.

(7) Pramanik, M.; Tsujimoto, Y.; Malgras, V.; Dou, S. X.; Kim, J. H.; Yamauchi, Y. Mesoporous iron phosphonate electrodes with crystalline frameworks for lithium-ion batteries. *Chem. Mater.* **2015**, *27*, 1082−1089.

(8) Kim, Y.; Goodenough, J. B. Lithium insertion into transition-metal monosulfides: Tuning the position of the metal 4s band. *J. Phys. Chem. C* **2008**, *112*, 15060−15064.

(9) Tong, W.; Yoon, W.-S.; Hagh, N. M.; Amatucci, G. G. A novel silver molybdenum oxyfluoride perovskite as a cathode material for lithium batteries. *Chem. Mater.* **2009**, *21*, 2139−2148.

(10) Brec, R.; Ouvrard, G.; Louisy, A.; Rouxel, J.; Lemehaute, A. The influence, on lithium electrochemical intercalation, of bond ionicity in layered chalcogenophosphates of transition metals. *Solid State Ionics* **1982**, *6*, 185−190.

(11) Li, B.; Wang, D.; Wang, Y.; Zhu, B.; Gao, Z.; Hao, Q.; Wang, Y.; Tang, K. One-step synthesis of hexagonal $TiOF_2$ as high rate electrode material for lithium-ion batteries: research on Li intercalation/de-intercalation mechanism. *Electrochim. Acta* **2015**, *180*, 894−901.

(12) Wang, M.; Weng, G.-M.; Yasin, G.; Kumar, M.; Zhao, W. A high-performance tin phosphide/carbon composite anode for lithium-ion batteries. *Dalton Trans.* **2020**, *49*, 17026−17032.

(13) Liu, X. -Y.; Najam, T.; Yasin, G.; Kumar, M.; Wang, M. One-pot synthesis of high-performance tin chalcogenides/C anodes for Li-ion batteries. *ACS Omega* (Just Accepted).

(14) Kuzminskii, Y. V.; Voronin, B. M.; Redin, N. N. Iron and nickel phosphorus trisulfides as electroactive materials for primary lithium batteries. *J. Power Sources* **1995**, *55*, 133−141.

(15) Fujii, Y.; Miura, A.; Rosero-Navarro, N. C.; Higuchi, M.; Tadanaga, K. $FePS_3$ electrodes in all-solid-state lithium secondary batteries using sulfide-based solid electrolytes. *Electrochim. Acta* **2017**, *241*, 370−374.

(16) Dangol, R.; Dai, Z.; Chaturvedi, A.; Zheng, Y.; Zhang, Y.; Dinh, K. N.; Li, B.; Zong, Y.; Yan, Q. Few-layer $NiPS_3$ nanosheets as bifunctional materials for Li-ion storage and oxygen evolution reaction. *Nanoscale* **2018**, *10*, 4890−4896.

(17) Du, C.-F.; Liang, Q.; Yan, Q. Graphene-supported bimetal phosphorus trisulfides as novel 0D-2D nanohybrid for high rate Li-ion storage. *J. Energy Chem.* **2018**, *27*, 190−194.

(18) Edison, E.; Chaturvedi, A.; Ren, H.; Sreejith, S.; Lim, C. T.; Madhavi, S. Route of irreversible transformation in layered tin thiophosphite and enhanced lithium storage performance. *ACS Appl. Energy Mater.* **2018**, *1*, 5772−5778.

(19) Foot, P. J. S.; Katz, T.; Patel, S. N.; Nevett, B. A.; Pieecy, A. R.; Balchin, A. A. The structures and conduction mechanisms of lithium-intercalated and lithium-substituted nickel phosphorus trisulphide ($NiPS_3$), and the use of the material as a secondary battery electrode. *Phys. Status Solidi A* **1987**, *100*, 11−29.

(20) Park, M.-H.; Kim, K.; Kim, J.; Cho, J. Flexible dimensional control of high-capacity Li-ion-battery anodes: From 0D hollow to 3D Porous germanium nanoparticle assemblies. *Adv. Mater.* **2010**, *22*, 415−418.

(21) Wang, X.-L.; Han, W.-Q.; Chen, H.; Bai, J.; Tyson, T. A.; Yu, X.-Q.; Wang, X.-J.; Yang, X.-Q. Amorphous hierarchical porous GeO_x as high-capacity anodes for Li ion batteries with very long cycling life. *J. Am. Chem. Soc.* **2011**, *133*, 20692−20695.

(22) Jo, G.; Choi, I.; Ahn, H.; Park, M. J. Binder-free Ge nanoparticles−carbon hybrids for anode materials of advanced lithium batteries with high capacity and rate capability. *Chem. Commun.* **2012**, *48*, 3987−3989.

(23) Xue, D.-J.; Xin, S.; Yan, Y.; Jiang, K.-C.; Yin, Y.-X.; Guo, Y.-G.; Wan, L.-J. Improving the electrode performance of Ge through Ge@C core-shell nanoparticles and graphene networks. *J. Am. Chem. Soc.* **2012**, *134*, 2512−2515.

(24) Wang, M.; Zheng, H.; Zhan, W.; Luo, Q.; Tang, K. Facile scalable synthesis of carbon-coated Ge@C and GeX@C (X=S, Se) anodes for high performance lithium-ion batteries. *ChemistrySelect* **2019**, *4*, 6587−6592.

(25) Seng, K. H.; Park, M.-H.; Guo, Z. P.; Liu, H. K.; Cho, J. Self-assembled germanium/carbon nanostructures as high-power anode

material for the lithium-ion battery. *Angew. Chem., Int. Ed.* **2012**, *51*, 5657−5661.
(26) Peng, W.; Li, J.; Shen, K.; Zheng, L.; Tang, H.; Gong, Y.; Zhou, J.; Chen, N.; Zhao, S.; Chen, M.; Gao, F.; Gou, H. Iron-regulated NiPS for enhanced oxygen evolution efficiency. *J. Mater. Chem. A* **2020**, *8*, 23580−23589.
(27) Khan, A. A.; Khan, I.; Ahmad, I.; Ali, Z. Thermoelectric studies of IV-VI semiconductors for renewable energy resources. *Mater. Sci. Semicond. Process.* **2016**, *48*, 85−94.
(28) Chao, J.; Wang, Z.; Xu, X.; Xiang, Q.; Song, W.; Chen, G.; Hu, J.; Chen, D. Tin sulfide nanoribbons as high performance photoelectrochemical cells, flexible photodetectors and visible-light-driven photocatalysts. *RSC Adv.* **2013**, *3*, 2746−2753.
(29) Sung, G.-K.; Park, C.-M. Puckered-layer-structured germanium monosulfide for superior rechargeable Li-ion battery anodes. *J. Mater. Chem. A* **2017**, *5*, 5685−5689.
(30) Han, J.-T.; Huang, Y.-H.; Goodenough, J. B. New anode framework for rechargeable lithium batteries. *Chem. Mater.* **2011**, *23*, 2027−2029.
(31) Chen, J. S.; Lou, X. W. D. SnO_2-based nanomaterials: Synthesis and application in lithium-ion batteries. *Small* **2013**, *9*, 1877−1893.
(32) Lou, X. W.; Chen, J. S.; Chen, P.; Archer, L. A. One-pot synthesis of carbon-coated SnO_2 nanocolloids with improved reversible ithium storage properties. *Chem. Mater.* **2009**, *21*, 2868−2874.
(33) Zhang, J.; Cui, R.; Li, X. a.; Liu, X.; Huang, W. A nanohybrid consisting of $NiPS_3$ nanoparticles coupled with defective graphene as a pH-universal electrocatalyst for efficient hydrogen evolution. *J. Mater. Chem. A* **2017**, *5*, 23536−23542.
(34) Li, X.; Xin, M.; Guo, S.; Cai, T.; Du, D.; Xing, W.; Zhao, L.; Guo, W.; Xue, Q.; Yan, Z. Insight of synergistic effect of different active metal ions in layered double hydroxides on their electrochemical behaviors. *Electrochim. Acta* **2017**, *253*, 302−310.
(35) Peng, B.; Xu, Y.; Liu, K.; Wang, X.; Mulder, F. M. High-performance and low-cost sodium-ion anode based on a facile black phosphorus-carbon nanocomposite. *ChemElectroChem* **2017**, *4*, 2140−2144.
(36) Kim, Y.; Hwang, H.; Lawler, K.; Martin, S. W.; Cho, J. Electrochemical behavior of Ge and GeX_2 (X = O, S) glasses: Improved reversibility of the reaction of Li with Ge in a sulfide medium. *Electrochim. Acta* **2008**, *53*, 5058−5064.
(37) Wei, Y.; He, J.; Zhang, Q.; Liu, C.; Wang, A.; Li, H.; Zhai, T. Synthesis and investigation of layered GeS as a promising large capacity anode with low voltage and high efficiency in full-cell Li-ion batteries. *Mater. Chem. Front.* **2017**, *1*, 1607−1614.
(38) Zhang, F.; Xia, C.; Zhu, J.; Ahmed, B.; Liang, H.; Velusamy, D. B.; Schwingenschlögl, U.; Alshareef, H. N. $SnSe_2$ 2D anodes for advanced sodium ion batteries. *Adv. Energy Mater.* **2016**, *6*, 1601188.
(39) Xia, W.; Wang, H.; Zeng, X.; Han, J.; Zhu, J.; Zhou, M.; Wu, S. High-efficiency photocatalytic activity of type II SnO/Sn_3O4 heterostructures via interfacial charge transfer. *CrystEngComm* **2014**, *16*, 6841−6847.
(40) Qu, B.; Zhang, M.; Lei, D.; Zeng, Y.; Chen, Y.; Chen, L.; Li, Q.; Wang, Y.; Wang, T. Facile solvothermal synthesis of mesoporous Cu_2SnS_3 spheres and their application in lithium-ion batteries. *Nanoscale* **2011**, *3*, 3646−3651.
(41) Zhang, K.; Zhang, T.; Liang, J.; Zhu, Y.; Lin, N.; Qian, Y. A potential pyrrhotite (Fe_7S_8) anode material for lithium storage. *RSC Adv.* **2015**, *5*, 14828−14831.
(42) Xue, H.; Yu, D. Y. W.; Qing, J.; Yang, X.; Xu, J.; Li, Z.; Sun, M.; Kang, W.; Tang, Y.; Lee, C.-S. Pyrite FeS_2 microspheres wrapped by reduced graphene oxide as high-performance lithium-ion battery anodes. *J. Mater. Chem. A* **2015**, *3*, 7945−7949.
(43) Wen, Z.; Cui, S.; Kim, H.; Mao, S.; Yu, K.; Lu, G.; Pu, H.; Mao, O.; Chen, J. Binding Sn-based nanoparticles on graphene as the anode of rechargeable lithium-ion batteries. *J. Mater. Chem.* **2012**, *22*, 3300−3306.
(44) Wang, Z.; Wang, Z.; Liu, W.; Xiao, W.; Lou, X. W. Amorphous $CoSnO_3$@C nanoboxes with superior lithium storage capability. *Energy Environ. Sci.* **2013**, *6*, 87−91.

https://doi.org/10.1021/acsomega.1c01042
ACS Omega 2021, 6, 17247−17254